metals

MDPI

Article

Formation Mechanisms of Chilled Layer on the Perimeter of Superalloy Seed

Yangpi Deng [1,2], Dexin Ma [1,*], Jianhui Wei [1,2], Yunxing Zhao [1,2], Lv Li [1,2], Bowen Cheng [1,2] and Fuze Xu [1,2]

[1] State Key Laboratory for Powder Metallurgy, Central South University, Changsha 410083, China; dengyp@wedge.com.cn (Y.D.); weijianhui@csu.edu.cn (J.W.); zhaoyx1@wedge.com.cn (Y.Z.); lil1@wedge.com.cn (L.L.); chengbw@wedge.com.cn (B.C.); xufuze12@csu.edu.cn (F.X.)
[2] Shenzhen Wedge Aviation Technology Co., Ltd., Shenzhen 518045, China
* Correspondence: madexin@csu.edu.cn

Abstract

The seeding technique is the only way to precisely control the crystal orientation of single-crystal superalloy castings. However, an inevitable assembly gap exists between the seed and the mold cavity in practice, whose role in defect formation remains insufficiently understood. To elucidate the mechanism and impact of this gap, superalloy seeds were machined to different extents, aiming to create varying gaps with the mold. After the seeding experiment, the chilled layers formed on the perimeter of the pre-processed seeds were detected, exhibiting two distinct microstructural zones: a eutectic aggregation region at the bottom and an equiaxed grain at the top. The thicker the layer, the more pronounced the differences in microstructure between these two regions. This can be explained by the fact that during preheating, the γ/γ' eutectic-rich interdendritic region (enriched with Al + Ti + Ta) in the original seed melted first due to its lower melting point. The molten fluid flowed downward into the gap, solidifying rapidly into the chilled layer. The leading portion of the fluid, melting from the interdendritic zone, formed the eutectic zone in the lower part of the chilled layer. The subsequently poured charge alloy melt (non-enriched with Al + Ti + Ta) generated the upper equiaxed zone with only a little γ/γ' eutectic. These equiaxed grains in the chilled layer subsequently grew upward and potentially developed into stray grains of the casting.

Keywords: superalloy; single-crystal; seed; chilled layer; eutectic

Check for updates

Academic Editor: Maciej Motyka

Received: 5 December 2025
Revised: 7 January 2026
Accepted: 8 January 2026
Published: 11 January 2026

Copyright: © 2026 by the authors. Licensee MDPI, Basel, Switzerland. This article is an open access article distributed under the terms and conditions of the Creative Commons Attribution (CC BY) license.

1. Introduction

Turbine blades, serving as the most critical hot-section components in aero-engines, are subjected to extreme service conditions, such as high temperature, high pressure, and complicated loads. Single-crystal (SC) superalloys, characterized by superior high-temperature mechanical properties and oxidation resistance, have been widely utilized in the casting of turbine blades [1–8]. SC superalloys contain more than ten alloying elements and exhibit an intricate microstructure. In particular, γ/γ' eutectic is an essential constituent of the microstructure in SC superalloys, which forms within the interdendritic regions. The solidification of eutectic can be summarized into three mechanisms [9–14]: (1) nucleation from the interdendritic residual liquid, (2) nucleation on the primary γ phase, and (3) nucleation on the MC-type carbide. The content and distribution of the eutectics are influenced by the alloy composition, solidification conditions, and casting geometry [15–22]. Seo et al. [15] suggested that minor compositional differences in total γ'-forming elements

induced remarkable differences in the γ/γ' eutectic fraction between CMSX-6 and CMSX-10. In addition, the elements Re and Hf also affect the eutectic structure. With the increase in the contents of Re and Hf, the amount of the γ/γ' eutectics increases significantly. In particular, the addition of Re leads to the substantial enrichment of the γ/γ' eutectic-forming elements such as Al and Ta in the liquid phase between dendrites. Additionally, an increase in Hf content results in a higher volume fraction of the γ' phase. Both of these elements are favorable for the formation of the eutectic [17–20]. The upward accumulation phenomenon of eutectic structure during directional solidification of superalloy castings was reported [21,22], which could be due to the upward solutal flow of eutectic-forming elements through diffusion and convection. Meanwhile, utilizing a novel pull-up method to achieve top–down directional solidification, the eutectic accumulation in directionally solidified superalloys can be effectively eliminated.

The fabrication of single-crystal superalloy turbine blades primarily relies on two techniques: grain selection method and seeding technique. The grain selection technique can only approximately control the primary crystal orientation (<001>) of single-crystal castings. In contrast, the seeding technique was widely used to fabricate the SC superalloy blades to three-dimensionally control the crystal orientation of the SC castings. This method employs a pre-oriented seed crystal with precisely defined primary and secondary crystallographic orientations, which is positioned within a cavity at the bottom of the mold. During heating and holding, the upper part of the seed undergoes partial remelting. Subsequently, the molten metal is poured and directional solidification via epitaxial growth from the residual seed then occurs, thereby resulting in a single-crystal casting with the desired orientation [23–26]. In the seeding process, the seed state is important for the successful epitaxial crystal growth of SC blades [27]. Zhao et al. [28] investigated the influence of the crystallographic orientation of the seed on the crystal growth of superalloy. The results showed that when the initial dendrites deviated significantly from the axial direction, the undercooling caused by the deviation between dendrites and heat flow direction could lead to the formation of stray grains. In some studies, thin-substance mixed Al_2O_3 and SiO_2 particles were detected on the surface of the seed, causing solidification defects such as low-angle grains and other unfavorable grains during the directional solidification [29]. Hu's research [30] demonstrated that the smaller primary dendrite spacing of the seed was beneficial for reducing melt convection in the mushy zone and preventing dendrite deformation. The author of this article previously discovered that the pre-deformation of the seeds might lead to the accumulation of residual stress on the seed surface, which subsequently induced recrystallization grains and served as the origin of the new stray grains [31]. Previous investigations have predominantly concentrated on the influencing factors such as the crystallographic orientation of the seed, its alloy composition and the solidification parameters. However, the impact of the seed's assembly state on epitaxial growth has received limited attention in the literature.

In actual production of SC castings with the seeding technique, the seed surface is ground to remove the oxide scale and to ensure smooth insertion into the seed cavity of the shell mold. Therefore, the seed diameter is slightly smaller than the inner diameter of the seed cavity, inevitably resulting in a gap between the seed and the mold. It should also be noted that the dimensions of the seed are influenced by manual handling. Excessive removing can lead to an enlarged gap at the seed–mold interface, whose impact on grain defects has not been systematically investigated. In this study, the seeds with different gap sizes to the mold were utilized to investigate their effects on the seeding process for preparation of SC superalloy castings.

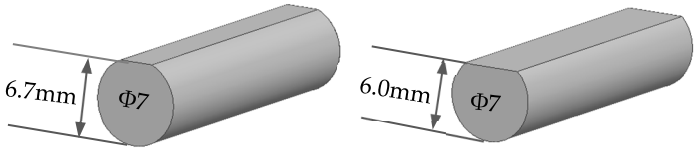
2. Materials and Methods

In this experiment, the second-generation superalloy DD419 was used as the seed and casting material. The alloy composition is listed in Table 1. The SC rods of 7 mm in diameter with orientation basically parallel to the [001] crystal direction (with a deviation angle of less than 10°) were selected as the seeds and cut to a specific length. Before casting, the ceramic shell molds were prepared using the investment casting method, with the casting cavity in the upper part and a tubular seed cavity with an open hole at the bottom.

Table 1. Chemical composition of Ni-based superalloy DD419 (wt.%).

Cr	Co	Mo	W	Re	Al	Ti	Ta	Hf	W + Re	Al + Ti + Ta	Ni
6.56	9.38	0.65	6.27	2.94	5.56	1.08	6.47	0.13	9.21	13.11	Bal.

In industrial practice, a small but inevitable gap on the order of 0.1 mm typically exists between the seed and the mold cavity to allow for assembly and accommodate thermal expansion. In this study, to systematically amplify and investigate the effects of this gap, we intentionally created larger gaps of approximately 0.3 mm and 1.0 mm. Wire electrical discharge machining was used to cut a flat surface along the axial direction of two sets of seeds (Figure 1) before inserting the seeds into the cavity with depths of 0.3 mm (seed A) and 1.0 mm (seed B), respectively. Subsequently, both types of seeds were ground to remove the oxide layer and machined marks from the surface. These process after wire cutting will not compromise the seed crystals' surface quality. Simultaneously, this operation aligns with the pretreatment procedures for seeds before daily routine casting, ensuring that the surface quality of the seeds in this experiment remains consistent with that of seeds used in routine casting production.



(**a**) (**b**)

Figure 1. Schematic diagram of the prepared seeds: A (**a**) and B (**b**).

Five samples of each seed, A and B, were selected for the casting experiment. The seeds with the same length were inserted into the same shell mold to, respectively, create gaps of approximately 0.3 mm and 1.0 mm between the seeds and the inner surface of the mold. The seeds were fixed with the mold by applying ceramic slurry on the bottom. The slurry was deposited exclusively as a thin layer, ensuring no interference with local heat dissipation between the seeds and the water-cooled chill plate. Additionally, the slurry had a composition similar to that of the mold shell and remained solid during the entire pouring process, which would not infiltrate into the gap between the seed crystal and the mold shell.

As shown in Figure 2, the shell mold inserted with seeds was positioned on a water-cooled chill plate and then elevated into the heating chamber of the furnace for directional solidification. The preheating and casting temperatures were both set at 1550 °C, with the mold held at this temperature for 15 min before pouring. Subsequently, the poured mold was withdrawn from the heating zone at a rate of 3 mm/s. After removing the shell mold and cutting off the gating system, two sets of specimens were obtained, referred to as specimen A and specimen B according to the seed shape. These samples were then macroetched to examine their surface morphology. Trans-

verse and longitudinal sections were cut from the seed crystals and etched in a solution of 500 mL HCl + 500 mL H_2O + 350 g $FeCl_3 \cdot 6H_2O$. The microstructures of these sections were observed using an optical microscope (OM, NIKON, Tokyo, Japan) and a scanning electron microscope (SEM, FEI Company, Hillsboro, OR, USA). The chemical compositions of the corresponding areas were also analyzed by an energy-dispersive spectrometer (EDS, EDAX, Pleasanton, CA, USA). Furthermore, ImageJ software (version 1.52) was employed for the analysis of the graphical data. To ensure the statistical reproducibility of the experimental results, five samples for each specimen type (A and B) were prepared and analyzed. All microstructural observations were performed on at least three different viewing fields per sample.

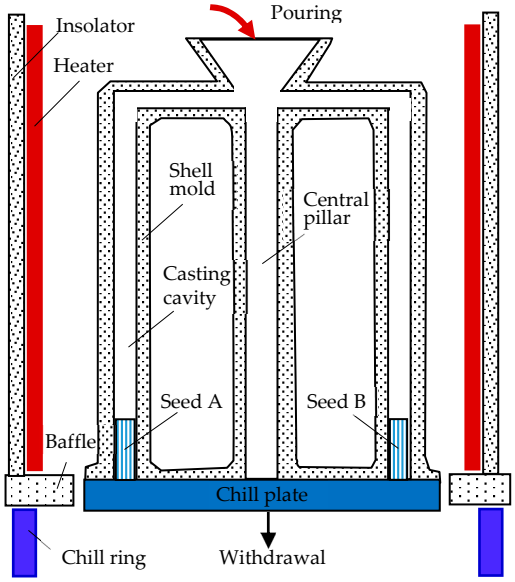


Figure 2. Schematic of the mold cluster inserted with seeds and placed on the chill plate in the furnace for pouring and directional solidification.

3. Results and Discussion

3.1. The Surface Morphology of the Chilled Layer

Figure 3a,b shows the typical surface morphology of specimen A and specimen B at the lower part of the seeding zones after etching. The left ends of both specimens correspond to the bottom of the unmelted seeds. Above these, a layer adhering to the seed surface can be seen, with a length of approximately 30 mm. The surfaces of the layers both exhibit fine equiaxed grains. Owing to the gap between the seed and the shell mold, the molten metal from the upper part of the seed flowed down into the gap in the heating process of the furnace. However, since the bottom of the seeds contacted with the water-cooled plate and thus remained at a lower temperature, the seeds failed to melt completely. Furthermore, the molten metal in the gap also solidified at a certain height instead of reaching the bottom, and then formed the chilled layer.

The right parts of both specimens in Figure 3 are the directional solidification zones above the chilled layers, revealing light and serious columnar stray grains, respectively. In specimen A (Figure 3a), the matrix of the directional solidification zone consists of directionally grown dendrites, which were essentially unaffected by the chilled layer. Only a slightly deviated grain grew into the specimen, forming a low-angle grain boundary. In contrast, specimen B (Figure 3b) shows multiple large-angle deviated grains in the directional solidification zone, covering the specimen surface and continuing to grow through the entire casting. Consequently, these unfavorable grain defects would lead to the formation of the polycrystalline structure instead of a single-crystal one.

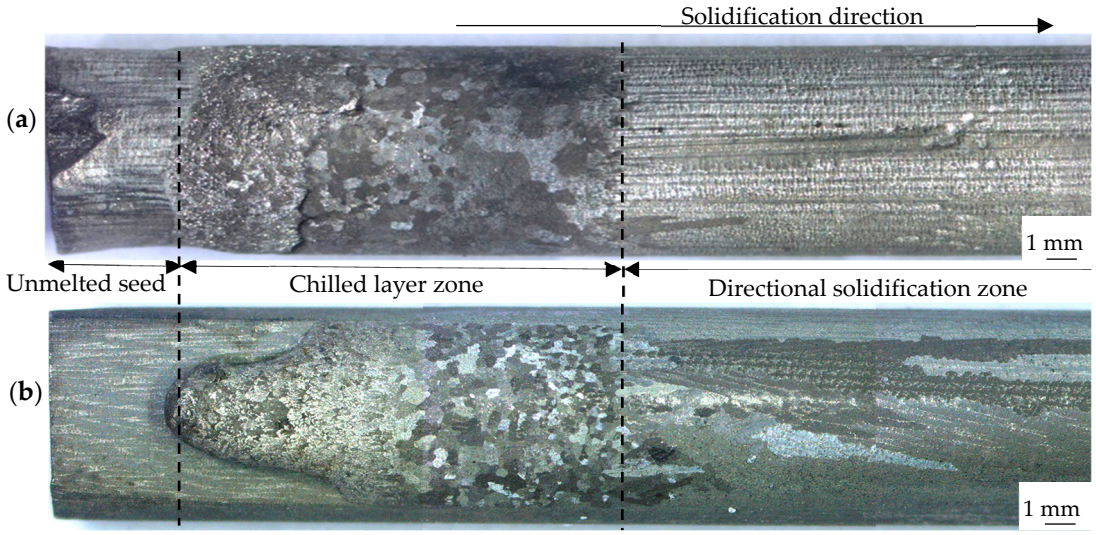


Figure 3. Photographs of specimen A (**a**) and specimen B (**b**) at the lower part of the seeding zones, revealing the typical morphology of the chilled layers.

3.2. The Longitudinal and Cross-Sectional Microstructure of the Chilled Layer

3.2.1. Specimen A (Smaller-Gap Seed)

Figure 4 presents the longitudinal section of the chilled layer of specimen A (Figure 4a) and the corresponding local magnifications (Figure 4(b1–b3)). It can be detected that the thickness of the chilled layer is approximately 200 μm, showing an entirely distinct morphology from that of the internal matrix. Based on the microstructural characteristics, the chilled layer can be divided into two zones. The lower region (referring to the left in Figure 4a) is described as the eutectic aggregation zone (or eutectic zone for short) due to the presence of a large amount of γ/γ' eutectic microstructure. The upper part of the chilled layer is referred to as the equiaxed grain zone, because it is primarily composed of the equiaxed γ-phase grains. The eutectic amount in this equiaxed zone is significantly lower than that in the eutectic zone, and is, meanwhile, similar to that in the internal matrix of the specimen.

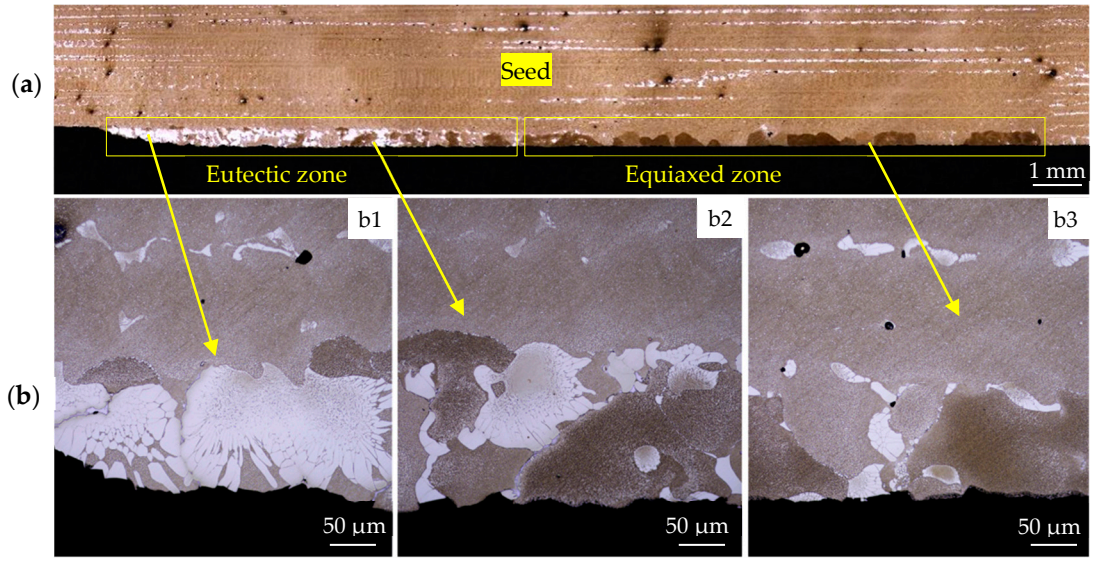


Figure 4. The longitudinal section of the chilled layer of specimen A (**a**) and the corresponding local magnifications (**b**) corresponding to: (**b1**) the lower eutectic zone, (**b2**) the upper eutectic zone, and (**b3**) the equiaxed zone.

3.2.2. Specimen B (Larger-Gap Seed)

Figure 5 partly shows the longitudinal section (Figure 5a) and three transverse sections (Figure 5b) of specimen B. The chilled layer is approximately 1 mm thick and similarly comprises two regions clearly: the lower eutectic zone and the upper equiaxed zone. In comparison to specimen A (Figure 4), specimen B has a recognizable boundary between the eutectic zone and the equiaxed zone in the chilled layer. It is interesting to note that the eutectic microstructure in the lower part of the eutectic zone is significantly coarser (Figure 5(b1)) than that in the upper part (Figure 5(b2)). The bottom of the layer is droplet-shaped and has no connection with the unmelted seed. This can be explained by the fact that as the molten alloy flowed down along the gap, its temperature decreased and its fluidity deteriorated. Under the effects of gravity and surface tension, the fluid front solidified into a droplet shape.

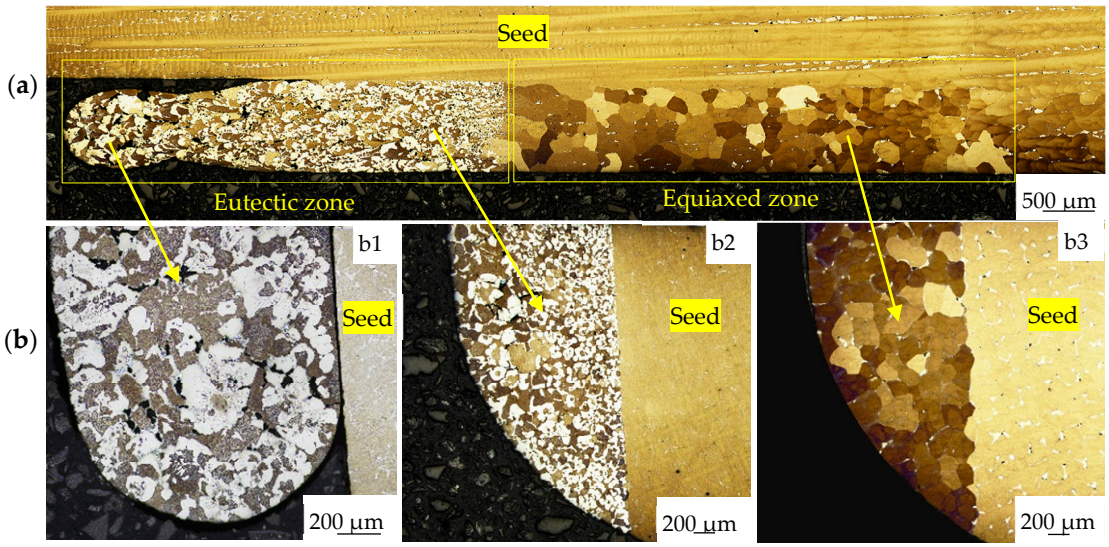


Figure 5. The longitudinal section (**a**) and the transverse ones (**b**) of the chilled layer of specimen B corresponding to: (**b1**) the lower eutectic zone, (**b2**) the upper eutectic zone, and (**b3**) the equiaxed zone.

The transverse section at the lower part of the eutectic zone in the chilled layer is depicted in Figure 5(b1), where a gap exists between the layer and the unmelted seed. The γ/γ' eutectic here is abundant and severely coarse. It can be deduced that although the temperature around this height was already low, the droplet of flowing metal was unable to dissipate its heat quickly because of the ineffective contact with the surrounding seed. As a result of the slow cooling rate, the γ/γ' eutectic in the droplet became very coarse.

Figure 5(b2) exhibits the transverse section at the upper part of the eutectic zone in the chilled layer. The layer is closely bonded to the seed, indicating that the temperature at this height was relatively high. The molten alloy flowing down had good fluidity, filling the gap between the shell mold and the seed. This intimate contact with the metallic seed facilitated rapid heat transfer from the liquid alloy, promoting the finer solidified microstructure. Notably, those eutectics near the seed were more refined, demonstrating the quenching effect of the seed for the solidification of the alloy fluid in the gap. According to the simulation work by Hu [32], before the directional solidification stage, the temperature of the seed was lower than that of the mold. The molten alloy in contact with the seed experienced a higher cooling rate and nucleation undercooling. As a result, the eutectic structure near the seed was finer compared to the other side in Figure 5(b2).

By using the software ImageJ, the eutectic proportion in Figure 5(b1,b2) was measured to be approximately 52.7% and 61.4%, respectively. These ratios in the eutectic zone of the chilled layer are significantly higher than the typical γ/γ' fraction of 5% in DD419 castings.

In Figure 5(b3), the transverse section of the equiaxed zone of the chilled layer is depicted, exhibiting a microstructure distinct from the eutectic zone shown in Figure 5(b1,b2). The molten alloy partially merged with the seed and re-nucleated into heterogeneous oriented γ-phase grains due to the quenching effect of the seed. In comparison, the γ/γ' eutectic phase is sparse and smaller in size, similar to that of the seed matrix. During the subsequent withdrawal process, these randomly oriented γ-grains in the equiaxed zone grow into stray grains; so, the monocrystallinity of the SC casting is destroyed. Stray grain defects caused by the chilled layer on the helical selector section have also been reported [33].

SEM images of the transverse sections in Figure 5(b1–b3) are correspondingly shown in Figure 6a–c, revealing the γ/γ' eutectic microstructure in the lower and upper parts of the eutectic zone and in the equiaxed zone of the chilled layer. The lower part of the eutectic zone contains large, sunflower-like eutectic structures (Figure 6a), while the upper part consists of significantly finer eutectics (Figure 6b). In the equiaxed zone (Figure 6c), only a few eutectic structures are dispersedly distributed between the γ-phase grains.

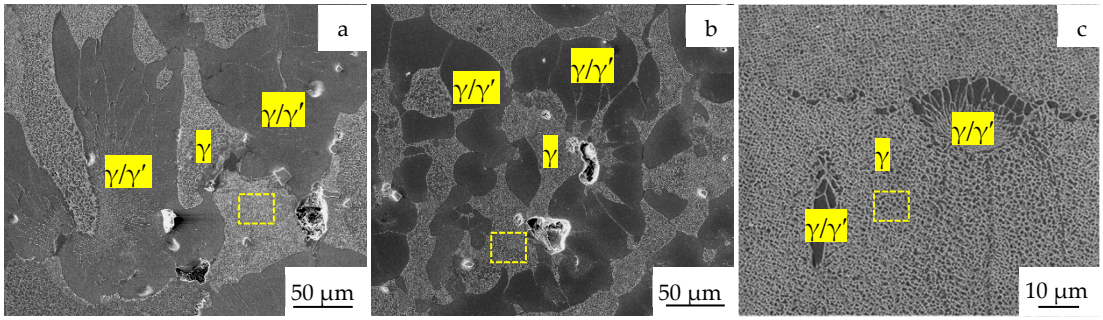


Figure 6. Magnified SEM images (**a**), (**b**), and (**c**) corresponding to Figure 5(b1–b3), respectively, illustrating the eutectic microstructure in each zone.

Figure 7a–c presents the enlarged SEM micrographs of γ grains corresponding to the dashed-box regions in Figure 6a–c, displaying the γ'-phase precipitated on the γ-phase matrix. In the eutectic zone, as can be seen in Figure 7a,b, γ'-phase particles have an irregular cubic morphology, large but non-uniform sizes, similar to the interdendritic structure in typical castings. It can be deduced that a high concentration of γ'-forming elements such as Al, Ti, and Ta was achieved in this zone, just as in the interdendritic region of castings. On the contrary, in the upper equiaxed zone (Figure 7c), the precipitated γ'-phase particles are small, predominantly cubic, and uniformly distributed. This suggests a deficiency in Al, Ti, and Ta elements, which hinders γ' particle precipitation. The size of the γ'-phase particles in this equiaxed zone (Figure 7c) was measured to be only 0.28 μm, while the γ' size in the eutectic zone (Figure 7a,b) was 1.5 μm and 1.2 μm, respectively.

The measured fraction of γ/γ' eutectic structures and the size of γ' particles precipitated on the γ matrix are listed in Table 2. EDS elemental mapping was conducted on the eutectic and equiaxed zones to detect the average elemental distribution, and these results are also presented in Table 2. The data reveal a significant aggregation of eutectic structures in the eutectic zone of the resolidified layer, with the γ/γ' phase accounting for over 50% of the total composition. This is attributed to the enrichment of γ'-forming elements such as Al, Ti, and Ta in this region. The upper and lower eutectic zones exhibit similar eutectic fractions but differ in eutectic size. Compared to the equiaxed zone, the total content of γ'-forming elements (Al + Ti + Ta) in the eutectic zone is 38% higher than

that in the equiaxed zone, whereas the total content of γ′-inhibiting elements (W + Re) in the eutectic zone is approximately 40% lower than that in the equiaxed zone, finally causing a γ/γ′ fraction about 10 times higher.

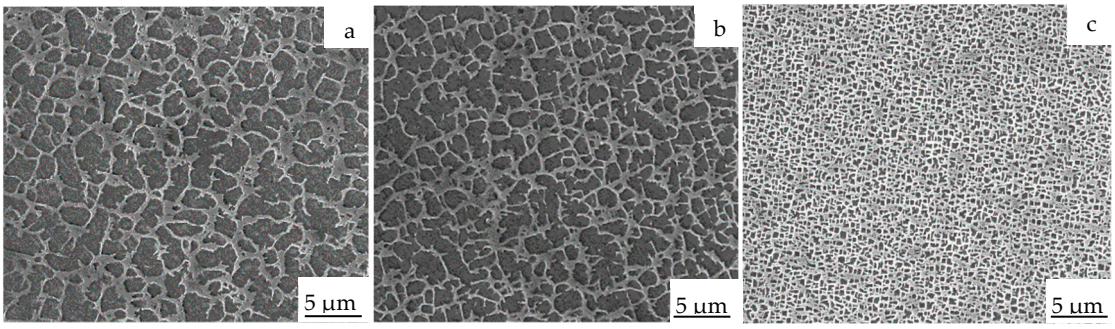


Figure 7. Magnified SEM images (**a**), (**b**), and (**c**) corresponding to the dashed-box regions in Figure 6a–c, respectively, illustrating the γ′-phase particles precipitated on the γ-phase matrix in each zone.

Table 2. Measurement results in the different regions of the chilled layer of specimen B.

Region	γ/γ′ Fraction	γ′-Size (μm)	Chemical Composition (wt. %)											
			Cr	Co	Mo	W	Re	Al	Ti	Ta	Hf	Ni	W + Re	Al + Ti + Ta
Eutectic zone (lower part)	52.7%	1.5	6.26	8.39	0.39	3.53	1.69	4.23	2.33	10.66	1.36	61.16	5.22	17.22
Eutectic zone (upper part)	61.4%	1.2												
Equiaxed zone	5.0%	0.28	6.80	9.59	0.36	5.65	2.81	3.39	1.54	7.52	1.12	61.22	8.46	12.45

The emergence of the γ/γ′ eutectic structures in the as-cast microstructure of superalloys is a consequence of non-equilibrium solidification, and it also reflects the degree of elemental segregation. The eutectic structure is formed in the residual liquid phase during the later stage of solidification. The eutectic transformation is initiated only when the concentration of γ′-forming elements (Al + Ti + Ta) in the residual liquid phase reaches a certain level and exceeds the eutectic composition point. Therefore, greater elemental segregation leads to a higher eutectic content [34]. It is just the different distributions of Al + Ti + Ta in the eutectic and equiaxed zones that cause the different content of eutectic structures in the chilled layer.

From the measurement data listed in Table 2, it can be seen that the composition of Al + Ti + Ta in the eutectic zone reaches 17.22%, which is higher than that in both the equiaxed zone (12.45%) and in the charge original alloy (13.11%, as shown in Table 1). This indicates a strong driving force both for the solidification of γ/γ′ eutectic from the residual liquid and for the precipitation of γ′ particles from the γ grain matrix in the eutectic zone. Consequently, the γ′ phase in this region exhibits relatively large dimensions. In contrast, elements W + Re are enriched in the equiaxed zone. It was reported that W would interact with Re, reducing the diffusion rate of γ′-forming elements and suppressing γ′ growth, thereby refining the γ′ phase [35–39]. As a result, the differences in the content of these elements between the two regions contribute to even more pronounced differences in γ′ phase size. Furthermore, the mechanisms for the inhomogeneous distribution of elements, especially Al + Ti + Ta, in the chilled layer will be discussed in detail in the following section.

In addition, EDS analysis in this study was performed not through point scanning but via area scanning across the entire region. The acquisition time per scan was maximized to ensure data reliability. The EDS measurement was controlled within an error of less than

10%. The measurement result can then be reasonably used to characterize the compositional differences between different structural zones.

4. Discussion

Based on the above experimental data, the formation mechanisms of the chilled layer can be illustrated through the schematic diagram in Figure 8 and described in the following stages.

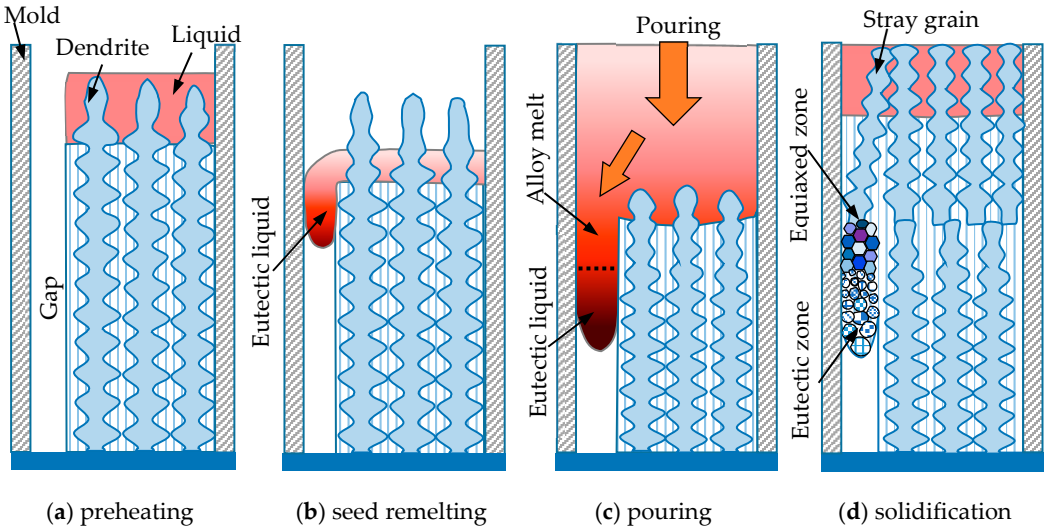


Figure 8. Schematic illustration of the formation process of the chilled layer on seed perimeter.

(1) During the preheating stage of the casting experiment, the top of the seed melts initially, preferentially beginning with the interdendritic regions (Figure 8a). This behavior is attributed to the solute redistribution during solidification, where the dendrite trunks were enriched with refractory elements W and Re. This gives the dendrite trunks a higher melting point. Conversely, the γ'-forming elements Al + Ti + Ta were expelled into the residual liquid between the dendrites, forming γ/γ' eutectics with a lower melting point [40,41]. Consequently, the interdendritic regions of the seed crystal, which contained a significant amount of γ/γ' eutectics, melt preferentially. This also leads to an enrichment of Al + Ti + Ta in the melt liquid.

(2) As the temperature gradually increased during preheating, the melt–back interface of the seed crystal progressively moved downward. Then, the molten alloy in the interdendritic regions accumulated gradually and flowed down slowly into the gap between the shell mold and the seed, driven by gravity (Figure 8b). This part of the fluid, which originated from the interdendritic regions of the seed, could be referred to as the eutectic liquid due to its enrichment with eutectic-forming elements Al + Ti + Ta.

(3) After preheating the shell mold, the overheated charge alloy melt in the crucible was poured into the mold, first filling the seed cavity at the bottom. It forced the eutectic liquid in the gap to flow down rapidly (Figure 8c). Upon cooling and solidification, this eutectic liquid ultimately developed into the eutectic zone of the lower chilled layer (Figure 8d). In more detail, the leading part of the eutectic liquid was in a semi-solid state initially and formed a suspended shape due to surface tension, without full contact with the seed crystal and the mold wall. As a consequence of the low cooling rate, the coarse eutectic structures at the bottom of the eutectic zone appeared. However, the latter part of the eutectic liquid adhered closely to the cold seed and formed finer eutectic structures because of effective heat dissipation. Above the eutectic liquid was the poured alloy melt, whose composition is the same as that of

the charge alloy, without enrichment of Al + Ti + Ta. It solidified upon contact with the seed crystal under rapid cooling, forming normal equiaxed γ-phase grains with normal eutectic fractions, constituting the equiaxed zone in the upper region of the chilled layer (Figure 8d).

(4) When the mold was pulled downward after pouring the alloy melt, the liquid above the remelting interface of the seed solidified upward in the form of columnar dendrites. However, equiaxed grains at the top of the chilled layer grew epitaxially, developing into stray grains with random orientations (Figure 8d). These grains subsequently evolved into stray grain defects during the withdrawal process, as observed in Figure 3, which destroyed the monocrystallinity of the SC casting. This formation mechanism of stray grains differs completely from the mechanism referenced in prior work by the authors [31], where stray grains originated from unmelted and recrystallized grains on the surface of the seed crystal.

In summary, the chilled layer formed on the seed perimeter comprises two distinct regions: a lower eutectic zone and an upper equiaxed zone. The eutectic zone originated from the low-melting-point interdendritic liquid of the seed, enriched with γ′-forming elements Al + Ti + Ta. During preheating, this so-called eutectic liquid flowed down slowly into the gap. The pouring of the charge alloy melt accelerated the downward movement of the eutectic liquid. In the lower portion, a coarse eutectic structure was formed due to the low cooling rate. In contrast, the upper portion of the eutectic liquid was in close contact with the seed and cooled rapidly, forming fine eutectic structures. Additionally, the formation of the equiaxed zone primarily arose from the charge alloy melt, along with melted dendrite core liquid residual and interdendritic liquid. This zone lacked Al + Ti + Ta but had a significant accumulation of W and Re, leading to the formation of equiaxed γ-phase grains with limited eutectics. These γ-grains grow epitaxially into columnar stray grains during subsequent directional solidification.

It should be noted that this study focuses on the second-generation superalloy DD419. For superalloys with lower Al + Ti + Ta contents, the volume fraction of eutectics is typically diminished. In such cases, the amount of low-melting-point eutectic in the interdendritic regions of the seed may decrease. Consequently, the volume of eutectic liquid flowing into the gap during the preheating stage could be correspondingly lower, leading to a reduction in both the thickness and enrichment level of the eutectic zone within the chilled layer. Nevertheless, interdendritic microsegregation is an inherent phenomenon in superalloy. As long as the segregation (with the enrichment of Al + Ti + Ta in the interdendritic regions) persists and a gap between the seed and the mold shell exists, the aforementioned chilled layer formation mechanism may still occur, but its severity may be mitigated with a reduction in the alloy's eutectic propensity.

In the manufacture of SC superalloy castings via the seeding technology, seed crystals are ground to remove surface oxides and ensure smooth insertion into the mold cavity. This process often gives rise to a smaller seed diameter compared to the mold's inner diameter, creating an inevitable gap between the seed and the mold wall. In this study, this gap was intentionally enlarged to systematically investigate how different gap sizes affect the formation of a chilled layer and stray grains, providing crucial insights for the seeding process of SC superalloy castings.

5. Conclusions

1. The gap between the seed and the mold wall can cause a chilled layer on the seed perimeter. A larger gap results in a thicker chilled layer and more severe stray grain defects. By using the seeds with an approximate 0.3 mm gap from the mold shell, the epitaxial growth of SC was essentially unaffected by the chilled layer, whereas

the castings prepared with an approximate 1.0 mm gap between the seed and mold exhibited multiple large-angle deviated grains from the chilled layer.

2. The chilled layer can be divided into two zones. The lower part is the γ/γ' eutectic zone, where the γ/γ' eutectic fraction exceeds 50%. The upper zone is characterized by equiaxed γ-phase grains containing only 5% γ/γ' eutectic structures, similar to normal as-cast structures.
3. The lower part of the eutectic zone, exhibiting a suspended shape and coarse γ/γ' eutectics, was formed due to slower heat dissipation. In contrast, the upper part of the eutectic zone was tightly bonded to the unmelted seed experienced rapid cooling, leading to fine eutectic structures.
4. The lower part of the chilled layer was enriched in γ'-forming elements Al + Ti + Ta, derived from the preferentially melted interdendritic regions of the seed during preheating, resulting in an abnormal eutectic zone. The upper chilled layer mainly originated from the subsequently poured charge alloy melt without enrichment in γ'-forming elements; consequently, no excessive γ/γ' eutectic development was observed.
5. During subsequent directional solidification, the equiaxed γ-grains in the chilled layer grew epitaxially into misoriented stray grains; so, the monocrystallinity of the SC casting was destroyed.

Author Contributions: Conceptualization, Y.D. and D.M.; methodology, Y.D. and D.M.; software, J.W.; validation, Y.Z. and L.L.; formal analysis, Y.D. and L.L.; investigation, B.C. and F.X.; resources, J.W.; data curation, F.X.; writing—original draft preparation, Y.D.; writing—review and editing, Y.D. and D.M.; visualization, Y.Z. and B.C.; supervision, D.M.; project administration, Y.Z.; funding acquisition, J.W. All authors have read and agreed to the published version of the manuscript.

Funding: This research was funded by the Shenzhen Science and Technology Program (JSGG20220831092800001).

Data Availability Statement: The original contributions presented in this study are included in the article. Further inquiries can be directed to the corresponding author.

Conflicts of Interest: Author Yangpi Deng, Jianhui Wei, Yunxing Zhao, Lv Li, Bowen Cheng and Fuze Xu was employed by the company Shenzhen Wedge Aviation Technology Co., Ltd. The remaining author declares that the research was conducted in the absence of any commercial or financial relationships that could be construed as a potential conflict of interest.

References

1. Donachie, M.J.; Donachie, S.J. *Superalloys: A Technical Guide*; ASM International: Troit, MI, USA, 2002; pp. 11–25.
2. Harris, K.; Erickson, G.L.; Schwer, R.E. *Metals Handbook*, 10th ed.; ASM International: Russell Township, OH, USA, 1990.
3. Meetham, G.W. *The Development of Gas Turbine Materials*; Applied Science Publishers: London, UK, 1981; pp. 89–119.
4. Reed, R.C. *The Superalloys Fundamentals and Applications*; Cambridge University Press: Cambridge, UK, 2006.
5. Yang, W.; Li, J.; Liu, S.; Wang, X.; Zhao, J.; Shi, Z. Effect of Low-Angle Boundaries on the Microstructures and Tensile Properties of the Third-Generation Single-Crystal Superalloy DD9. *Crystals* **2022**, *12*, 595. [CrossRef]
6. Epishin, A.; Fedelich, B.; Finn, M.; Künecke, G.; Rehmer, B.; Nolze, G.; Leistner, C.; Petrushin, N.; Svetlov, I. Investigation of Elastic Properties of the Single-Crystal Nickel-Base Superalloy CMSX-4 in the Temperature Interval between Room Temperature and 1300 °C. *Crystals* **2021**, *11*, 152. [CrossRef]
7. Gudivada, G.; Pandey, A.K. Recent developments in nickel-based superalloys for gas turbine applications: Review. *J. Alloys Compd.* **2023**, *963*, 171128. [CrossRef]
8. Jian, Z.; Wang, L.; Guang, X.; Dong, W.; Jian, S.; Lu, Y.; Huang, Y.; Li, Y. Recent Progress in Research and Development of Nickel-Based Single Crystal Superalloys. *Acta Metall. Sin.* **2023**, *59*, 1109–1124.
9. Bae, J.S.; Lee, J.H.; Kim, S.S.; Jo, C.Y. Formation of MC-γ/γ' eutectic fibers and their effect on stress rupture behavior in D/S Mar-M247LC superalloy. *Scripta Materis.* **2001**, *45*, 503–508. [CrossRef]
10. Wang, F.; Ma, D.; Bührig-Polaczek, A. Eutectic Formation During Solidification of Ni-Based Single-Crystal Superalloys with Additional Carbon. *Met. Mater. Trans. A* **2017**, *48*, 5442–5448. [CrossRef]

11. Moreira, M.F.; Fantin, L.B.; Azevedo, C.R.F. Microstructural Characterization of Ni-Base Superalloy As-Cast Single Crystal (CMSX-4). *Inter Metalcast.* **2021**, *15*, 676–691. [CrossRef]
12. D'Souza, N.; Dong, H. Solidification path in third-generation Ni-based superalloys, with an emphasis on last stage solidification. *Scr. Mater.* **2007**, *56*, 41–44. [CrossRef]
13. Seo, S.M.; Kim, I.S.; Lee, J.H.; Jo, C.Y.; Miyahara, H.; Ogi, K. Microstructural evolution in directionally solidified Ni-base superalloy IN792+Hf. *J. Mater. Sci. Technol.* **2008**, *24*, 110–114.
14. Park, K.; Withey, P. Compositions of Gamma and Gamma Prime Phases in an As-Cast Nickel-Based Single Crystal Superalloy Turbine Blade. *Crystals* **2022**, *12*, 299. [CrossRef]
15. Seo, S.M.; Lee, J.H.; Yoo, Y.S.; Jo, C.Y.; Miyahara, H.; Ogi, K. Comparative Study of the γ/γ' Eutectic Evolution During the Solidification of Ni-Base Superalloys. *Metall. Mater. Sci.* **2011**, *42*, 3150–3159. [CrossRef]
16. Homam, N. Microstructural investigation and castability anticipation in modern Ti/Al/Nb-containing nickel-based superalloys. *Trans. Nonferrous Met. Soc. China* **2016**, *26*, 1607−1619.
17. Pandey, P.; Sawant, A.K.; Nithin, B.; Peng, Z.; Makineni, S.K.; Gault, B.; Chattopadhyay, K. On the effect of Re addition on microstructural evolution of a CoNi-based superalloy. *Acta Mater.* **2019**, *168*, 37–51. [CrossRef]
18. Cao, L.; Zhou, Y.; Jin, T.; Sun, X. Effects of Re on surface eutectic formation for Ni-base single crystal superalloys during directional solidification. *J. Mater. Sci. Techno.* **2017**, *33*, 1308–1313. [CrossRef]
19. Zhao, Y.; Zhang, J.; Luo, Y.; Tang, D.; Feng, Q. Effects of Hf on High Temperature Low Stress Rupture Properties of a Second Generation Ni-based Single Crystal Superalloy DD11. *Acta Metall. Sin.* **2015**, *51*, 1261–1272.
20. Shi, Z.; Liu, S.; Yue, X.; Wang, Z.; Li, J. Effect of Re Content on Mircrostructure and Stress Rupture Properties of DD15 Single Crystal Superalloy. *Rare Met. Mater. Eng.* **2023**, *52*, 1977–1984.
21. Ma, D.; Zhao, Y.; Xu, W.; Pi, L.; Li, Z. Surface Effect on Eutectic Structure Distribution in Single Crystal Superalloy Castings. *Acta Metall. Sin.* **2021**, *57*, 1539–1548.
22. Ma, D.; Zhao, Y.; Xu, W.; Wang, F. Effect of Gravity on Directionally Solidified Structure of Superalloys. *Acta Metall. Sin.* **2023**, *59*, 1279–1290.
23. Wang, Q.; Yang, W.; Lin, S.; Liu, C.; Qin, J.; Qu, P.; Qu, P.; Zhang, J. A novel l12-strengthened single crystal high entropy alloy with excellent high-temperature mechanical properties. *Mater. Charact.* **2024**, *212*, 113958. [CrossRef]
24. Yang, S.; Bao, J.; Yang, X.; Zhen, Q.; Liu, Q.; Zhang, J.; Hu, S. Controlling crystal orientation of Ni-based single crystal superalloy by inclined seeding metho. *J. Mater. Eng.* **2025**, *53*, 63–69.
25. Yang, Z.; Hu, S.; Chen, Y.; He, M.; Li, W.; Bai, W.; Wang, X. Effect of Growth Orientation on Solidification Process of Nickel-Based Single Crystal Superalloy DD6. *Metall. Mater. Trans. A* **2025**, *56*, 2653–2664. [CrossRef]
26. Qin, J.; Hu, S.; Yang, W.; Qu, P.; Liu, C.; Wang, Q.; Zhang, J.; Liu, L. Oxidation behavior of Ni-20W and Ni-20W-20Cr heterogeneous seeds under different vacuum conditions. *Vacuum* **2024**, *229*, 113578. [CrossRef]
27. Toloraiya, V.N.; Orekhov, N.G.; Kablov, E.N. Advanced Method for Single Crystal Casting of Turbine Blades for Gas Turbine Engines and Plants. *Metal. Sci. Heat. Treat.* **2002**, *44*, 279–283. [CrossRef]
28. Zhao, X.; Liu, L.; Yang, C.; Li, Y.; Fu, H. Influence of crystal orientation on cellular growth of a nickel-base single crystal superalloy. *J. Alloys Compd.* **2011**, *509*, 9645–9649. [CrossRef]
29. Yang, W.; Hu, S.; Huo, M.; Sun, D.; Zhang, J.; Liu, L. Orientation controlling of Ni-based single-crystal superalloy by a novel method: Grain selection assisted by un-melted reused seed. *J. Mater. Res. Technol.* **2019**, *8*, 1347–1352. [CrossRef]
30. Hu, S.; Liu, L.; Yang, W.; Sun, D.; Huo, M.; Li, Y.; Huang, T.; Zhang, J.; Sun, H.; Fu, H. Inhibition of stray grains at melt-back region for re-using seed to prepare Ni-based single crystal superalloys. *Prog. Nat. Sci.* **2019**, *29*, 582–586. [CrossRef]
31. Deng, Y.; Ma, D.; Zhao, Y.; Xu, W.; Xu, F.; Li, L. Stray Grain Formation Mechanism During Seeding Process of Single Crystal Superalloy DD419. *Rare Met. Mater. Eng.* **2024**, *53*, 2042–2048.
32. Hu, S.; Zhao, Y.; Bai, W.; Wang, X.; Yin, F.; Yang, W.; Liu, L. Temperature Field Evolution of Seeding during Directional Solidification of Single-Crystal Ni-Based Superalloy Castings. *Metals* **2022**, *12*, 817. [CrossRef]
33. Ma, D.; Wang, F.; Sun, H.; Xu, W. Experimental Investigations on Stray Grain Defects in Single Crystal Castings of Superalloys. *Foundry* **2019**, *68*, 558–566.
34. Fan, Y.; Zhao, X.; Qiao, L.; Song, Y.; Zhou, Y.; Cheng, Y.; Zeng, S.; Yue, Q.; Xia, W.; Gu, Y.; et al. Microstructure evolution and stability of directionally solidified superalloys with varying γ' phase forming elements. *Mater. Today Nano* **2025**, *30*, 100637. [CrossRef]
35. Liu, G.; Liu, L.; Cheng, A.; Ge, B.; Zhang, J.; Fu, H. Influence of withdrawal rate on the microstructure of Ni-base single-crystal superalloys containing Re and Ru. *J. Alloys Compd.* **2011**, *509*, 5866–5872. [CrossRef]
36. Cheng, T.; Wang, Y.; Zhao, Y.; Lv, B.; Ma, D. Effect of solidification direction on microstructure and mechanical property of single crystal superalloy CMSX-4. *Mater. Charact.* **2022**, *202*, 112992. [CrossRef]
37. He, J.; Liu, C.; Dong, J.; Zhang, M. The effect of Mo and Ti elements on long-term microstructure stability of 617B nickel-base superalloy. *J. Alloys Compd.* **2020**, *821*, 153217.

38. Kearsey, R.M.; Beddoes, J.C.; Jones, P.; Au, P. Compositional design considerations for microsegregation in single crystal superalloy systems. *Intermetallics* **2004**, *12*, 903–910. [CrossRef]
39. Sudbrack, C.K.; Ziebell, T.D.; Noebe, R.D.; Seidmanet, D.N. Effects of a tungsten addition on the morphological evolution, spatial correlations and temporal evolution of a model Ni-Al-Cr superalloy. *Acta Mater.* **2008**, *56*, 448–463. [CrossRef]
40. Heckl, A.; Rettig, R.; Cenanovic, S.; Goken, M.; Singer, R.F. Investigation of the final stages of solidification and eutectic phase formation in Re and Ru containing nickel-base superalloys. *J. Cryst. Growth* **2010**, *312*, 2137–2144. [CrossRef]
41. Gong, L.; Chen, B.; Du, Z.; Zhang, M.; Liu, R.; Liu, K. Investigation of Solidification and Segregation Characteristics of Cast Ni-Base Superalloy K417G. *Mater. Sci. Technol.* **2016**, *34*, 127–136. [CrossRef]

Disclaimer/Publisher's Note: The statements, opinions and data contained in all publications are solely those of the individual author(s) and contributor(s) and not of MDPI and/or the editor(s). MDPI and/or the editor(s) disclaim responsibility for any injury to people or property resulting from any ideas, methods, instructions or products referred to in the content.